Catalysis Science & Technology

Accepted Manuscript

ROYAL SOCIETY OF CHEMISTRY

www.rsc.org/catalysis

Journal Name

ARTICLE

High Temperature-Water Gas Shift on Ni-Cu/CeO_2 Catalysts: Effect of Ceria Nano-Crystal Size on Carboxylate Formation

Received 00th January 20xx,
Accepted 00th January 20xx

DOI: 10.1039/x0xx00000x

www.rsc.org/

Eng Toon Saw,[a] Usman Oemar,[a] Ming Li Ang,[a] Hidajat Kus[a] and Sibudjing Kawi[*a]

Various controllable sizes of thermally stable CeO_2 nano-spheres were successfully synthesized via PVP-assisted hydrothermal method for study on effect of ceria crystal size in high temperature water gas shift reaction. A series of catalyst characterization techniques such as X-ray Diffraction (XRD), Field Emission Scanning Electron Microscope (FESEM), Brunauer, Emmett and Teller Surface area (BET), X-ray Photon Spectroscopy (XPS), Carbon monoxide-Temperature Programmed Reduction-Mass Spectrometry (CO-TPR-MS), and *in-situ* Diffuse Reflectance Infra-red Fourier Transform Spectroscopy (DRIFTS) was implemented to explore the intrinsic properties of ceria crystal size effect. The XRD, FESEM and BET results indicate that ceria with the largest particle size and smallest crystal size of 12nm shows high specific surface area of 50m^2/g after calcination at 700°C. After impregnation, high metal dispersion (15%) and high surface lattice oxygen are observed on Ni-Cu bimetallic catalyst supported on the largest ceria particle sizes. This Ni-Cu/CeO_2 catalyst presents high reaction rates with low apparent activation energy as compared to other Ni-Cu/CeO_2 catalysts, revealing the important effect of ceria crystal and Ni-Cu alloy sizes. Further study shows that the high intensity of carboxylate species on 5Ni5Cu/CeO_2 catalyst with the biggest ceria crystal size could be the inhibitor or the real intermediate species. In addition, the reaction mechanism strongly depends on the Ni-Cu surface composition.

Introduction

Ceria (CeO_2), a well-known rare-earth metal due to its unique properties are deployed in oxygen storage, sensors, catalysts, photo-luminances, solid oxide fuel cells, biological oxygen scavenging agents and other research fields.[1-13] The uniqueness of ceria has motivated researchers to perform extensive investigations of its peculiar properties in various research areas, particularly in catalysis. Several methods have been widely employed in synthesizing nano-size material such as homogenous precipitation, sol-gel, micro-emulsion, hydrothermal, and sono-chemical.[14-27] Among those methods, hydrothermal method has emerged as one of the promising methods in synthesizing uniform, dispersed, small ceria nanoparticle and a variety of morphological features.[28-30] Nano-crystal size ceria is notable in playing a critical role in affecting surface redox properties and formation of defects or surface oxygen vacancies especially in the catalysis field of research.[31-33]

In water gas shift (WGS) reaction, ceria acts as an active catalyst support to improve the metal-support interaction and promote water dissociation via redox properties to form labile OH/O/H species, surface oxygen vacancies, and defects sites.[34-37] These intrinsic properties play important roles in catalytic activity and reaction mechanism for WGS reaction. One of the most governing properties are concentration of surface active species. This property which can be quantitatively determined from the *in-situ* DRIFTS intensity and (steady-state isotopic transient kinetic analysis) SSITKA coupled with DRIFTS and mass spectroscopy analysis[38] strongly depends on particle sizes of catalyst support, composition, metal particle sizes and reaction temperature. Panagiotopoulou et al. reported the effect of support particle size on the reducibility of Pt/TiO_2 catalysts which can affect the WGS activity.[39] They have also shown that the partially reduced TiO_2 support (small TiO_2 particle size) created new sites for CO adsorption which are located at the metal-support interface. Au loaded metal ceria nano-rod can disperse gold nano-clusters very well and exhibit high catalytic activity and selectivity for low temperature WGS by creating more surface oxygen vacancies.[40] Additionally, this may imply that small metal size could possibly increase the concentration of oxygen vacancies. Furthermore, Xu et al. also disclosed that decreasing ceria crystal size enhances the formation of superoxide species which increases the surface oxygen.[41] Kugai et al. also revealed that Rh species are highly dispersed when the crystal size of ceria support is small.[42] These findings are generally observed on low temperature WGS.

Sintering and agglomeration of nano-particle such as ceria at high temperature reaction are remarkably unavoidable. Moreover, high calcination temperature further reduces the

[a] Department of Chemical and Biomolecular Engineering, National University of Singapore, 4 Engineering Drive 4, Singapore 119260. Email: chekawis@nus.edu.sg; Fax: (+65) 6779 1936; Tel: (+65) 6516 6312

Electronic Supplementary Information (ESI) available: [details of any supplementary information available should be included here]. See DOI: 10.1039/x0xx00000x

surface area of ceria, decreases the catalytic activity and diminishes the surface active species.[43, 44] This problem adversely affects the applications of ceria as a catalyst support for high temperature reactions such as steam reforming of hydrocarbon and high temperature WGS reaction. Thereore, it is necessary to develop the thermally stable ceria and study the effect of ceria nanoparticle size in catalyzing high temperature WGS reaction via the catalyst structures, surface active species and reaction mechanism.

To examine the WGS reaction mechanism and active surface species, several advanced techniques such as *in-situ* XPS, *in-situ* DRIFTS, *in-situ* operando EXAFS, transient isotopic and spectroscopic techniques are developed.[45-47] In addition to the application of advanced spectroscopy, kinetic measurements, microkinetic modeling and periodic density functional theory (DFT) calculations have also been performed to validate the proposed WGS reaction mechanism.[48, 49] Two general WGS mechanistic pathway have been proposed: redox mechanism (regenerative) and associative mechanism (carbonate, formate or carboxyl as intermediate species).[50, 51] Jacobs et al. has utilized modified SSITKA with DRIFTS method to identify the important intermediate (formate) species formed during WGS reaction.[52] In recent study, Efstathiou et al. has also presented that *in-situ* SSITKA-DRIFTS-mass spectroscopy could differentiate the "active" and "in-active" reaction intermediates species during WGS reaction and also elucidate the active sites of these reaction intermediates.[53] However, the WGS reaction mechanisms still remain controversial particularly on the dominant reaction pathway, real active sites and active reaction intermediates species.

In this study, three different sizes of thermally stable nano-sphere ceria up to 700°C were synthesized via polyvinylpyrrolidone (PVP)-assisted hydrothermal method with various ceria-precursor concentration and aging time. Ni-Cu bimetallic with molar ratio of 1 was subsequently impregnated on three synthesized ceria nano-spheres. The reason of impregnating Ni-Cu bimetallic as active metal was mainly due to the formation of Ni-Cu alloy catalyst in methane suppression via enhanced CO adsorption for high temperature WGS[54] as the commercial Fe-Cr catalyst has carcinogenic and toxicity nature of the chromium compounds. The roles of ceria nano-size as catalyst support in catalyzing high temperature WGS reaction was extensively investigated. The roles of ceria nanoparticle size were evaluated in the following aspects: (i) supported bimetallic sizes and structures; (ii) role of oxygen species and active surface species on different ceria nanoparticle sizes; (iii) reaction mechanism.

Experimental Section

Catalyst Preparation

The starting materials sources were $Ce(NO_3)_3.6H_2O$, PVP360K (polyvinylpyrrolidone with average mol. Wt 360,000), $Cu(NO_3)_2.3H_2O$ and $Ni(NO_3)_2.6H_2O$ supplied from Sigma Aldrich. The ceria nanoparticle was prepared by the PVP-360K assisted hydrothermal method with a variation of ceria concentrations and reaction times. Three different sizes of spherical ceria were synthesized in the range of 150-350nm, 400-800nm and 800-1200nm denoted as CeO_2 (1), CeO_2 (2) and CeO_2 (3) respectively (Figure S1-S3). CeO_2 (1), CeO_2 (2) and CeO_2 (3) were prepared with 13.5mM of ceria precursor, 22.5mM of ceria precursor and 22.5mM of ceria precursor respectively. The weight of PVP360K was kept at 2.25g for all the samples. The required amount of cerium precursor was initially dissolved into 90ml of deionized water. PVP-360K surfactant was then slowly added into the solution and stirred for several hours to obtain fully dissolved solution. Thereafter, the prepared solution was poured into homemade autoclave and aged at 140°C for 12, 48, and 96 hours for CeO_2 (1), CeO_2 (2) and CeO_2 (3), respectively. The samples were then centrifuged at 10,000 rpm for 20mins repeatedly for four times, dried at 100°C in oven for overnight, calcined in the Carbolite tube furnace at 700°C to remove all the surfactants for two hours using heating and cooling rates of 10°C/min. Nickel precursor and copper precursor with the molar ratio of 1 and the total weight of 10wt% were dissolved into the measured deionized water and stirred evenly. The catalyst support was then introduced into the solution and dried at 100°C. The catalyst was then calcined again at 450°C for four hours. The calcined catalysts with different sizes of ceria were denoted as 5Ni5Cu/CeO_2 (1), 5Ni5Cu/CeO_2 (2) and 5Ni5Cu/CeO_2 (3).

Catalyst Characterizations

The X-ray diffraction (XRD) patterns of all the ceria catalyst support and 5Ni5Cu/CeO_2 catalysts were collected in a step-scan mode at 2θ of 20-60° with step size of 0.02°/s and scanning rate of 0.5°/min via a Shimadzu XRD-6000 powder diffractometer, where Cu target Kα-ray (operating at 40kV and 30mA) was used as the X-ray source. For the reduced 5Ni5Cu/CeO_2 catalysts, a narrow scan was performed to collect the spectra at 2θ of 40-55°. The average crystal size was determined from the XRD peak broadening by the Scherrer's equation, $t = K\lambda/FWHM \cos\theta$, where t is the average dimension of crystallites along the [hkl] direction whereas λ is the wavelength of X-ray irradiation (1.543Å); θ is the position of the (hkl) diffraction peak; K is the scherrer constant which is usually taken as 0.9 and FWHM is the line width at half maximum height.

The textural properties of ceria catalyst support and 5Ni5Cu/CeO_2 catalyst were measured by using N_2 adsorption/desorption measurement (Quantachrome, Nova 4200e). The specific surface area and pore size distributions were calculated using Brunauer-Emmett-Teller (BET) and Barrett-Joyner-Halenda (BJH) methods respectively. The catalysts were initially degassed under helium at 250°C for a minimum of 12 hours to remove the impurities before measurement.

The morphology of the ceria catalyst supports, reduced 5Ni5Cu/CeO_2 catalysts and spent catalysts was visually observed using a field emission scanning electron microscope (FESEM) (JEOL JSM-6700F). Prior to the analysis, the samples

were pre-coated with Pt with the sputtering times of 30s at 30 mA.

For N_2O decomposition experiments, 100mg of 5Ni5Cu/CeO_2 catalyst were reduced at 450°C for 1 hour. The catalysts were then purged under Helium gas to remove weakly chemisorbed hydrogen at 90°C. For nickel-copper metal dispersion, 250µL of purified 95% N_2O was titrated until the N_2O decomposition reached saturation using Quantachrome ChemBET 3000 TPD/TPR system coupled with ThermoStar GSD 300 (Quadstar 422) mass spectrometer (MS). The catalysts were then cooled to room temperature and followed by the H_2-TPR to determine the amount of dispersed metal. One molecule of N_2O is assumed to be adsorbed in stoichiometry of two atoms of Cu and Ni on the catalyst surface. The detailed experimental procedure was provided in our previous report.[55]

Hydrogen-temperature programmed reduction (H_2-TPR) experiments were performed using Quantachrome ChemBET 3000 TPD/TPR system equipped with a thermal conductivity detector (TCD). 50mg of sample (ceria catalyst support or 5Ni5Cu/CeO_2 catalyst) was first degassed at 250°C for one hour under purified Helium. Thereafter, 5% of H_2 in N_2 gas mixture at a flow rate of 60ml/min was passed through the sample and the TPR profiles were obtained by heating the sample from ambient temperature to 950°C at a heating rate of 10°C/min. The output signal of the gas mixture was measured continuously using the TCD as a function of temperature and recorded by a microcomputer.

Carbon monoxide-temperature programmed reduction (CO-TPR-MS) experiment was performed using Quantachrome ChemBET 3000 TPD/TPR system coupled with ThermoStar GSD 300 (Quadstar 422) mass spectrometer (MS). 100mg of sample (ceria catalyst support or 5Ni5Cu/CeO_2 catalyst) was firstly reduced at 450°C for one hour with purified H_2 and then flushed under purified helium to ambient temperature. Thereafter, 5% of CO in He gas mixture at a flow rate of 60ml/min was passed through the sample and the TPR profiles were obtained by heating the sample from ambient temperature to 950°C at a heating rate of 10°C/min. The effluent gas was measured continuously using MS.

Field Emission Transmission Electron Microscopy (FETEM-EDX) was performed to observe the structure and size of the ceria catalyst support and 5Ni5Cu/CeO_2 catalyst. The images of the ceria catalyst support and 5Ni5Cu/CeO_2 catalyst were obtained using a JEOL JEM-2010 electron microscope, equipped with an OXFORD INCA EDS analyzer operating in the range of 100 to 400k eV. Generally, the sample was dispersed ultrasonically in ethanol for 2 min in order to obtain a homogenous dispersed solution. A drop of the solution was then applied onto a coated carbon gold grid, followed by drying at 60°C for 5min.

X-ray photoelectron spectroscopy (XPS) was performed on a Kratos AXIS Ultra by using Monochromatized Al Kα as the X-ray source (1486.71 eV) at a constant dwell time of 100ms and pass energy of 40 eV. The X-ray source was run at a reduced power of 75 watts (15 kV and 5 mA). The working pressure in the analysis chamber was maintained at $5x10^{-9}$ Torr. The core level signals were obtained at a photoelectron take off angle of 90°. In the sample preparation, the 5Ni5Cu/CeO_2 catalyst was first reduced and transferred to the glove-box to prevent the oxidation of the reduced catalysts. Thereafter, the reduced 5Ni5Cu/CeO_2 catalysts were mounted on the standard sample stubs using double-sided adhesive tapes. All the binding energies were referenced to the C 1s hydrocarbon peak at 284.60 eV.

The Fourier Transform infrared spectrometer was a Bruker V-70, equipped with a MCT detector. A reaction chamber (Harrick, Praying Mantis) fitted with ZnSe window, capable to operate at high temperature, served as the reactor for CO adsorption study. 50mg of the ceria catalyst support was firstly outgassed at 250°C with purified helium for an hour and then cooled down to 25°C. 50mg of 5Ni5Cu/CeO_2 catalyst was firstly activated by introducing purified H_2 at 450°C for an hour. Thereafter, the chamber was cooled to 25°C with a flow of purified helium to remove the remaining hydrogen. 5% of CO in purified helium was introduced into the reaction chamber to study the catalyst behavior starting from 25°C, 50°C to 600°C with 50°C as the temperature interval. At each temperature, 100 scans were taken to improve the signal to noise ratio and to ensure the reproducibility of the steady state condition. For each spectrum, CO adsorption was taken after 15mins to ensure the steady-state condition. Scans were taken at a resolution of 4 to give a data spacing of $1cm^{-1}$.

WGS reaction was conducted in a fixed-bed flow reactor system using ¼" OD stainless steel reactor. The reactor was placed inside a split tube furnace (Carbolite) which temperature was controlled by a 2416 PID temperature controller. A blank stainless steel is tested to show no activity for WGS reaction. Deionized water was supplied by a Shimadzu HPLC pump and vaporized in the heated gas line kept at 150°C before entering the reactor. The feed gas lines were insulated with insulation tape to avoid condensation of water vapor in the lines. A cooling jacketed condenser was installed at the reactor exit to collect water and a moisture trap was used to remove the left over moisture. 50mg of the 5Ni5Cu/CeO_2 catalyst was packed inside the reactor for each run and pre-reduced in the flowing hydrogen (10 ml/min) for one hour at 450°C. Then purified helium was used to purge out the remaining hydrogen before the reaction begin. The feed gas mixture contained 5mol% of CO, 25%mol of H_2O and the balance helium was used to make up the total gas flow rate to reach 50 ml/min. The reaction studies were performed in the temperature range from 300 to 500°C. The readings were taken when the reaction reached steady state. The effluent of the reactor was analyzed on-line using a HP6890 Series GC equipped with thermal conductivity detector and packed column (Hayesep D, 20ft x 1/8 in. SS, 100/120 mesh). Methane gas was detected in negligible quantities by the GC.

The catalyst performance was evaluated by catalyst activity (mol %) and is presented as CO conversion (X_{CO}) and defined as follows:

$$X_{CO} = \frac{[F_{CO}]_{in} - [F_{CO}]_{out}}{[F_{CO}]_{in}} \times 100\%$$

For turnover frequency (TOF) calculation and reaction rates studies, the total gas flow rate of 100ml/min with the diluted catalysts (diluted with powder SiO_2 quartz) was performed in order to keep the total CO conversion below than 10%. The reaction condition with a mixture of 7%CO, 22%H_2O, 20%H_2, 8.5%CO_2 and balance helium was used. The measurements were conducted at temperatures of 325 to 400°C. The reaction condition is similar to our previous publication[54] [in which it has no mass and heat transfer limitation according to Koros-Nowak (K-N) criterion.[56, 57] Similarly, Weisz-Prater analysis and Mears analysis can also be performed to ensure no mass and heat transfer limitation.[58] The TOF and reaction rates calculated was shown as:

$$TOF = \frac{mol\ of\ CO\ converted}{mol\ of\ surface\ metal \times time(s)}$$

$$Rate\ (r) = \frac{mol\ of\ CO\ converted}{metal\ surface\ area\ (m^2) \times time(s)}$$

Results

X-ray Diffraction (XRD) Measurement

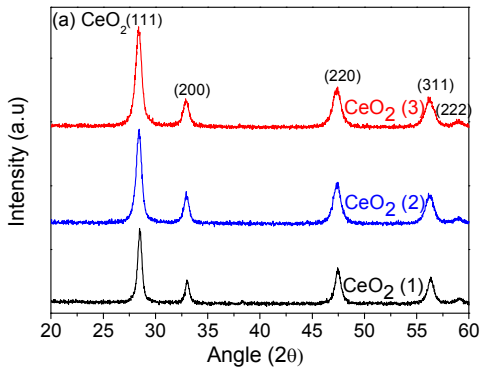

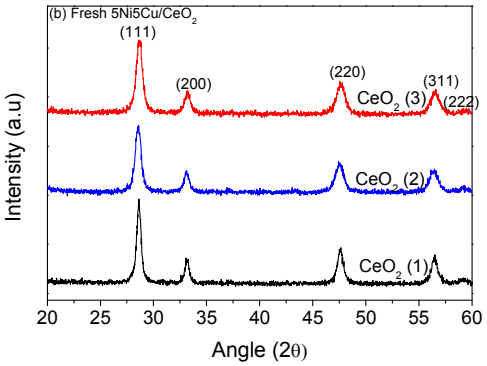

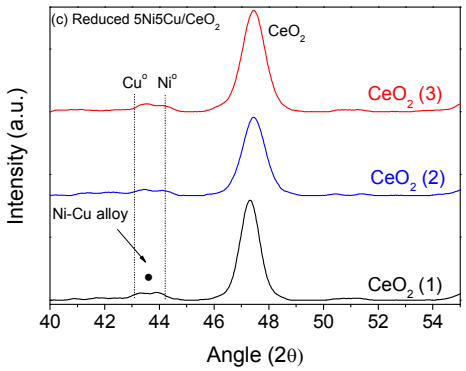

Fig. 1 XRD patterns for (a) Ceria nano-spheres; (b) 5Ni5Cu catalysts on ceria nano-spheres; (c) reduced 5Ni5Cu/CeO_2 catalysts.

Figure 1a depicts the XRD pattern of three different sizes of ceria after calcined at 700°C and measured at ambient temperature. All the ceria reveal the distinct and major peak of fluorite-type oxide structure of ceria (JCPDS 34-0394). The crystal size of ceria (Table 1) calculated using Scherrer equation shows decreasing size with order of 17.2nm, 13.9nm and 12.7nm for CeO_2 (1), CeO_2 (2) and CeO_2 (3) respectively. The crystal size of ceria has no significant change after Ni and

Table 1. Physicochemical properties of 5Ni5Cu supported on various sizes of ceria catalysts.

Catalyst	Ceria Crystal Size (nm)[a]	Ceria Particle Size (nm)[b]	S_{BET} (m^2/g)[c]	V_{pore} (cm^3/g)[d]	D_{pore} (nm)[d]	Ni-Cu Metal Surface Area (m^2/g)[e]	Metal Dispersion (%)[e]
CeO_2 (1)	17.2	150-350	39.3	0.033	3.41	-	-
CeO_2 (2)	13.9	400-800	44.5	0.047	3.75	-	-
CeO_2 (3)	12.7	800-1200	49.6	0.055	4.93	-	-
5Ni5Cu/CeO_2 (1)	17.9	-	16.9	0.026	6.41	73.7	11.4
5Ni5Cu/CeO_2 (2)	13.1	-	29.3	0.040	5.41	79.5	12.3
5Ni5Cu/CeO_2 (3)	12.8	-	36.7	0.040	4.32	98.2	15.1

[a] Calculated from XRD (Scherrer Equation); [b] Measured using FESEM; [c] Measured using BET method; [d] Measured using BJH method; [e] N_2O pulse titration.

Cu are impregnated onto ceria support and underwent thermal treatment (Figure 1b and Table 1).

The XRD pattern of reduced 5Ni5Cu/CeO_2 catalysts is shown in Figure 1c. According to literature, the diffraction 2θ at ~ 44.5° is corresponding to the presence of Ni° phase and a shift to lower 2θ values is possible for Ni-Cu bimetallic catalysts when Ni alloying with Cu species. Similarly, diffractions at 2θ = 43.4° is due to the presence of Cu° phase and a shift to higher 2θ values is possible for Ni-Cu alloy phase.[55, 59] From Figure 1c, it can be seen that all the three catalysts have the diffractions between 43.4 and 44.5. Thus, these diffractions are possibly corresponding to the presence of Ni-Cu alloy phases in the reduced forms of 5Ni5Cu/CeO_2 catalysts. Furthermore, the broadness of Ni-Cu alloy peak suggests that the Cu and Ni composition during alloy phase formation is not uniform. This broadness also makes it almost impossible to measure the crystallite size of Ni-Cu alloys in the reduced catalysts. Thus, N_2O decomposition was performed over reduced 5Ni5Cu/CeO_2 catalysts to measure the metal dispersion and surface area of all catalysts and the results are presented in Table 1. The 5Ni5Cu/CeO_2 (3) catalyst shows high metal dispersion of 15.1% followed by 5Ni5Cu/CeO_2 (2) catalyst and 5Ni5Cu/CeO_2 (1) catalyst which shows metal dispersion of 12.3% and 11.4% respectively. The calculated Ni-Cu metal surface areas were 73.7, 79.5 and 98.2 $m^2.g^{-1}$, respectively for reduced 5Ni5Cu/CeO_2 (1), 5Ni5Cu/CeO_2 (2) and 5Ni5Cu/CeO_2 (3) catalysts. Furthermore, the N_2O decomposition experiments over reduced CeO_2 support (Figure S4 to S6) shows that most of the N_2O is decomposed on reduced Ni and Cu species.

Catalyst Morphology (FESEM)

Figure 2a and 2b illustrate the FESEM images of calcined ceria and reduced 5Ni5Cu/CeO_2 catalysts. The particle size of ceria supports size ranges from 150-350nm, 400-800nm and 800-1200nm for CeO_2 (1), CeO_2 (2) and CeO_2 (3) respectively and the detail distribution can be seen in the supporting information (Figure S1 to S3). The Ni-Cu bimetallic particles are clearly observed to be attached on all ceria. The Ni-Cu bimetallic particle sizes distributions are depicted in Figure S7 to S9. The mean particle sizes of Ni-Cu bimetallic are shown as 22.4nm, 29.4nm and 28.3nm for 5Ni5Cu/CeO_2 (1), 5Ni5Cu/CeO_2 (2) and 5Ni5Cu/CeO_2 (3) respectively.

Textural Properties of Catalysts Supports (Ceria) and Catalysts

The textural properties of ceria and catalysts are summarized in Table 1. With increasing concentration of ceria precursor, the specific surface area of ceria catalyst support also increases with the following trend: 39.3 m^2/g for CeO_2 (1)< 44.5 m^2/g for CeO_2 (2)< 49.6 m^2/g for CeO_2 (3). The ceria pore volume and pore size also increase with increasing particle size of ceria. These results are in agreement with the XRD results which show that CeO_2 with bigger particle size and smaller crystal size of CeO_2 has high specific surface area and pore volume. This phenomena can be explained because increasing concentration ratio of ceria precursor to surfactant and aging time can enhance the growth rates of particle size (the easiness of the interaction among the nuclei ceria). Upon calcination at high temperature under oxygen rich atmosphere, the big size ceria synthesized with low concentration ratio of ceria precursor to surfactant is easily oxidized, leading to formation of big crystal size. Conversely, the small size ceria synthesized from high concentration ratio of ceria precursor to surfactant is probably due to the relatively low amount of surfactant to be oxidized, preventing the growth of the crystal size during high calcinations temperature. After the loading of Ni-Cu bimetallic, the specific surface areas and pore volume of the catalysts are reduced to 16.9 m^2/g, 29.3 m^2/g and 36.7 m^2/g for 5Ni5Cu/CeO_2 (1), 5Ni5Cu/CeO_2 (2) and 5Ni5Cu/CeO_2 (3) respectively, probably due to covering of the Ni-Cu bimetallic into the pore of the catalyst.

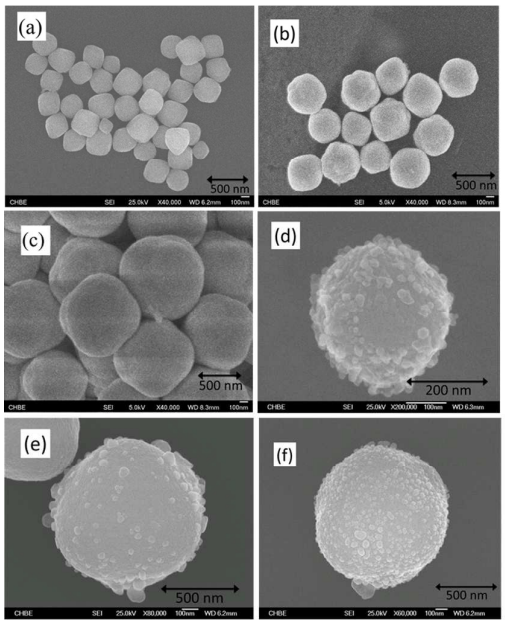

Fig. 2 FESEM Images for (a) CeO_2 (1); (b) CeO_2 (2); (c) CeO_2 (3); (d) reduced 5Ni5Cu/CeO_2 (1) catalyst; (e) reduced 5Ni5Cu/CeO_2 (2) catalyst; (f) reduced 5Ni5Cu/CeO_2 (3) catalyst.

H_2-TPR Measurement

Asdd Surface lattice oxygen of ceria plays a significant role in catalysis particularly in CO oxidation reaction. In order to determine the surface lattice oxygen and bulk lattice oxygen of ceria, H2-TPR was performed. Figure 3a shows the H2-TPR profile of three sizes of calcined ceria. It can be seen that two main peaks of hydrogen consumption are observed which low temperature (500-600°C) and high temperature (800-900°C) reduction peaks are attributed to surface lattice oxygen and bulk lattice oxygen respectively.60 The reduction peak at low temperature for CeO2 (1) is observed to be slightly higher than the reduction peak for CeO2 (2) and CeO2 (3) at 545°C, possibly due to the difficulty of bigger crystal size of CeO2 (1)

to be reduced as compared to CeO2 (2) and CeO2 (3).41, 61 This finding is in agreement with Johnson and Mooi, implying that hydrogen consumption is related to specific surface area of ceria.62

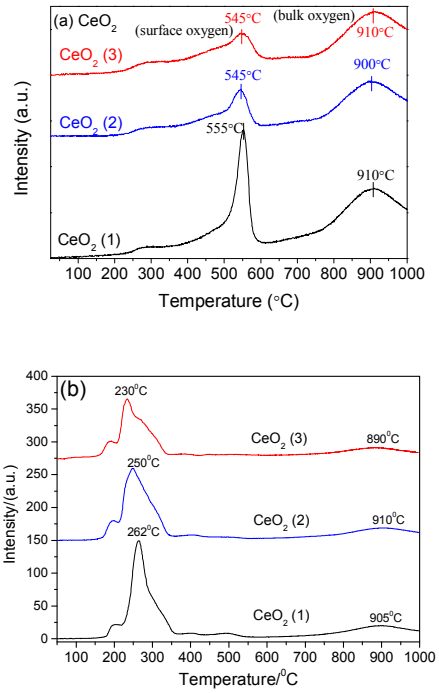

Fig. 3 H_2-TPR profiles for (a) ceria nano-spheres; (b) 5Ni5Cu/CeO_2.

The H_2-TPR profiles of the Ni-Cu catalysts impregnated on the prepared CeO_2 are shown in Figure 3b. It can be clearly seen that the H_2-TPR profiles exhibit the same hydrogen consumption peaks. In addition to the hydrogen consumptions corresponding to CeO_2 support, Figure 3 (b) also have two more hydrogen consumptions below 350°C. The lowest reduction temperature centered around 200°C for all the patterns are possibly due to reduction of surface Cu species. The high specific surface area ceria (small crystal size), 5Ni5Cu/CeO_2 (3) catalyst exhibits the next reduction temperature peak at 230°C, followed by 250°C and 262°C for 5Ni5Cu/CeO_2 (2) and 5Ni5Cu/CeO_2 (1) respectively, indicating that the reducibility of the catalysts increase with increasing specific surface area of ceria (decreasing crystal size of ceria). Besides, it is most preferable to form smaller Ni-Cu bimetallic particle size with small ceria crystal size as catalyst support.[39] The reduction of ceria can also be enhanced by addition of a small amount of noble metal or base metal which has been reported in literature.[34, 63, 64] In short, small Ni-Cu bimetallic particles is preferentially formed on small crystal size of ceria, resulting in improvement on reducibility of ceria.[54]

X-ray Photoelectron Spectroscopy (XPS) Measurement

The XPS spectra of the pure ceria and reduced catalysts were measured in the ultra-high vacuum condition at ambient condition. The surface composition of each element was calculated using respective deconvoluted peak area. Special attention is needed to quantify the surface composition of Ce^{3+}/Ce^{4+} based on the method reported by Zhang et al.[65] The ceria 3d spectra can be deconvoluted into 10 peaks where Ce^{4+} consists of six peaks (labeled as 882.6eV, 889.1eV, 897.1eV, 901.2eV, 907.7eV and 951.1eV) and Ce^{3+} occupies of four peaks (denoted at 880.8 eV, 886.9eV, 899.3 eV and 905.8eV). The concentration of Ce^{3+} was determined based on the total peak area of Ce^{3+} divided by the summation of the total peak area of Ce^{3+} and Ce^{4+}. Figure 4(i-a) displays O1s spectra for calcined ceria for three sizes of crystal sizes. There are two main O1s binding energies observed for all the ceria supports. The The BE at ~ 529eV is possibly due to the presence of lattice oxygen species while the BE at ~ 531eV is due to the presence of either oxygen vacancy or surface hydroxyl species.[13, 66, 67] The percentage amount of oxygen species summarized in Table 2 shows that CeO_2 (3) occupy lower oxygen lattice species as compared to CeO_2 (1). However, CeO_2 (3) has slightly more oxygen vacancy around 41.5% as compared to other CeO_2 catalyst support and in turn exhibits low percentage of ion Ce^{3+} content. This finding is in agreement with the Xu et al.[41] A slight shift of O1s to lower binding energy was observed from CeO_2 (1) to CeO_2 (3) which the ceria crystal size decreases from 17.2 to 12.7 nm, probably due to the lattice expansion of CeO_2 in oxygen vacancy formation and increase in concentrations of point defects.[13, 65, 68]

Figure 4(ii-a) to (ii-c) show the Cu2p, Ni2p and Ce3d XPS spectra for the reduced 5Ni5Cu/CeO_2 catalysts respectively. The Cu2p spectra and Ni2p spectra show shifting to lower binding energy from 932.4eV (Cu^o/Cu^+) to 932eV and 852.3eV (Ni^o) to 852eV respectively; whereas Ce3d spectra show

Table 2. Surface composition derived from XPS.

Catalyst	Oxygen Species			Percentage (Ce^{3+}/Ce^{4+})		Surface Composition (wt%)				Nickel/Copper Ratio
	O_L (Ce-O)	O_v (vacancy)	O_c (chemisorb)	Ce^{3+}	Ce^{4+}	O	Cu	Ni	Ce	Ni/Cu
CeO_2 (1)	62.2	37.8	-	30.5	69.5	-	-	-	-	-
CeO_2 (2)	63.1	36.9	-	26.5	73.5	-	-	-	-	-
CeO_2 (3)	58.5	41.5	-	26.5	73.5	-	-	-	-	-
5Ni5Cu/CeO_2 (1)	-	-	-	29.3	70.7	22.3	5.2	4.4	68.1	0.85
5Ni5Cu/CeO_2 (2)	-	-	-	28.2	71.8	20.5	6.6	5.8	67.1	0.87
5Ni5Cu/CeO_2 (3)	-	-	-	26.6	73.4	54.9	4.1	4.7	36.3	1.15

shifting to higher binding energy from 881.6eV to 882eV.[42, 69] This confirms the Ni-Cu alloy formation (Cu2p and Ni2p spectra) withdrawing electrons from ceria support.[70] Although the ceria size is varied, the formation of Ni-Cu alloy is observed for all catalysts. However, there is a variation on the surface composition of the Ni/Cu ratios as tabulated in Table 2. As ceria crystal size decreases, Ni to Cu ratio is increased slightly from 0.85 to 1.15, implying Ni-rich of Ni-Cu alloys are formed. According to Naghash et al., as ratio of Ni/Cu approaches 1, copper has a tendency to be segregated in order to minimize the interface surface energy.[69] However, our results are not in agreement with Naghash et al. for small crystal size of ceria. This could be due to the strong interaction between Cu-Ce as compared to Ni-Ce when Ni-Cu supported on ceria with small crystal size and big particle size. In addition, Ni ensemble on Cu is an efficient water-gas shift reaction in water dissociation and avoiding CO activation based on density functional theory calculations.[71]

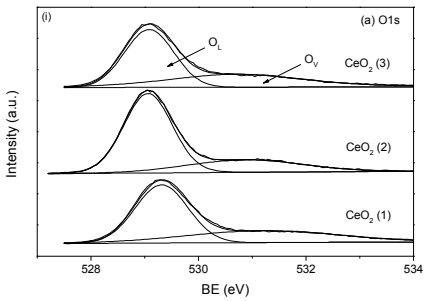

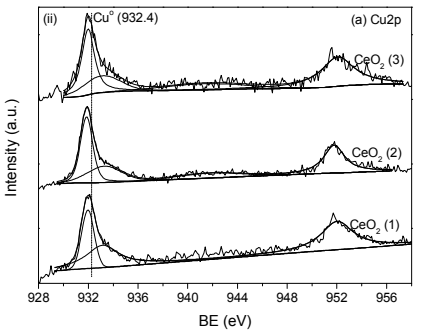

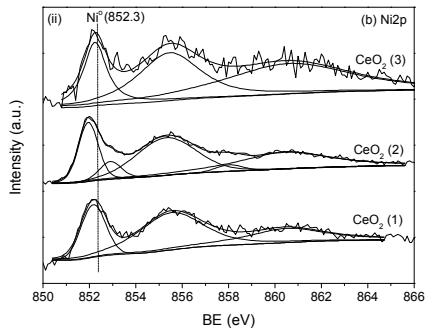

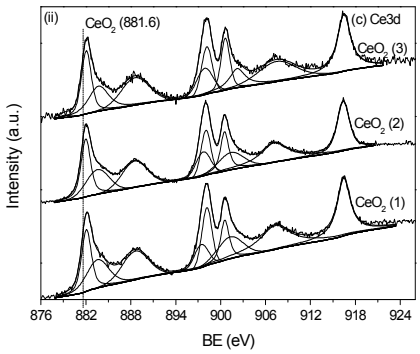

Fig. 4 XPS patterns for (i) Ceria nano-sphere, (a) O1s; (ii) Reduced catalyst 5Ni5Cu/CeO_2 (a) Cu2p, (b) Ni2p and (c) Ce3d.

Catalyst Activity

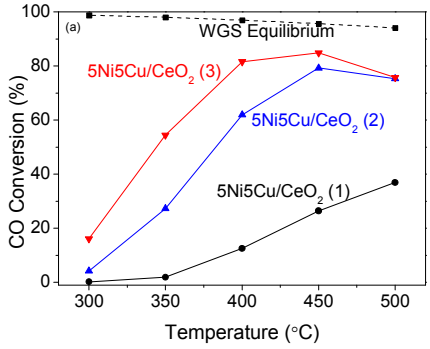

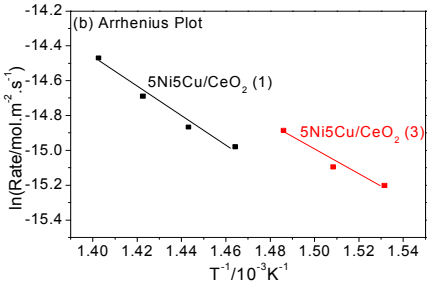

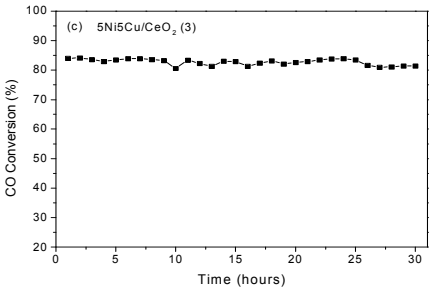

Fig. 5 (a) Catalytic Activity for three types of catalysts (reaction conditions: 5%CO, 25%H_2O, balance He); (b) Arrhenius plot for 5Ni5Cu/CeO_2 (1) and 5Ni5Cu/CeO_2 (3)

catalysts (reaction conditions: 7%CO, 22%H_2O, 8.5%CO_2, 20%H_2, balance He); (c) Stability Test for 5Ni5Cu/CeO_2 (3) at 450°C for 30 hours (reaction conditions: 5%CO, 25%H_2O, balance He).

The effect of ceria nanoparticle size was investigated in high temperature WGS reaction. The WGS reaction was performed from 300°C to 500°C with interval temperature of 50°C. As shown in Figure 5a, 5Ni5Cu/CeO_2 (3) catalyst exhibits the highest CO conversion along the reaction temperature from 300°C to 500°C, followed by 5Ni5Cu/CeO_2 (2) and 5Ni5Cu/CeO_2 (1). The highest CO conversion of 84% is reached at 450°C for 5Ni5Cu/CeO_2 (3) catalyst. This is possibly due to the formation of small Ni-Cu bimetallic size and high specific surface area of ceria (small crystal size) as shown in the XRD measurement. The catalytic activity shows the importance of Ni-Cu bimetallic size and specific surface area of ceria.

The turnover frequency (TOF) of Ni-Cu bimetallic catalysts of various sizes are shown in Table 3. The TOF value of Ni-Cu bimetallic catalyst on smaller ceria crystal size (5Ni5Cu/CeO_2 (3), 0.014 s^{-1}) is almost same as that on bigger ceria crystal size (5Ni5Cu/CeO_2 (1), 0.012 s^{-1}), showing that the TOF is not much depends on the ceria nanoparticle sizes. However, the normalized reaction rates for Ni-Cu bimetallic size summarized in Arrhenius plot (Figure 5b) clearly show that the reaction rates are depend on the ceria nanoparticle sizes and increases with decreasing ceria crystal size (17.9 nm to 12.8 nm) and increasing ceria specific surface area in the presence of product gases (H_2 and CO_2). Moreover, it is interested to note that the apparent activation energy of the reaction also varies slightly depending on the ceria sizes. The apparent activation energy decreases from ~69 kJ/mole for 5Ni5Cu/CeO_2 (1) catalyst to ~58 kJ/mole for 5Ni5Cu/CeO_2 (3) catalyst. Catalyst stability test is also performed at 450°C for 5Ni5Cu/CeO_2 (3) catalyst as shown in Figure 5c. There is slight decrease in catalyst activity (about 4%) is observed for 5Ni5Cu/CeO_2 (3) catalyst within 30 hours of reaction. The 5Ni5Cu/CeO_2 (3) spent catalyst (after 30 hours of reaction) was also further characterized by FESEM to identify any sintering of Ni-Cu bimetallic particle (shown in Figure 6). The spent catalyst of Ni-Cu bimetallic particle size (33.9 nm) is found to have slight increase in particle size as compared to the reduced 5Ni5Cu/CeO_2 (3) catalyst (28.3 nm) shown in Figure S10. This could be one of the reasons for showing slight decrease in catalytic performance for 5Ni5Cu/CeO_2 (3) catalysts during 30 hours of reaction time. FETEM-EDX is further utilized to identify the structure of Ni and Cu species after WGS reaction at 450°C for 30 hours. Figure 7 reveals that Ni-rich Ni-Cu alloy structure could be the main structure in catalyzing the WGS reaction which is shown in 'red' region for nickel element, 'green' region for copper element and 'blue' region for ceria element. This structure is in line with the XPS surface composition analysis as tabulated in Table 2. To sum up, it could be predicted that the Ni-rich Ni-Cu alloy bimetallic particle size is playing a governing role in affecting reaction rates and possibly the Ni-Cu bimetallic particle size in affecting the concentration of active reaction intermediates or species during water gas shift reaction.

Table 3. Comparison of water gas shift rates of 5Ni5Cu/CeO_2 catalysts of different sizes with other literature findings and the conventional catalyst.

Catalyst	Conditions	T/°C	E_a/kJmol^{-1}	TOF	Rate (10^{-6} mol/m^2.s)	Reference
5Ni5Cu/CeO_2 (3)	7%CO,22%H_2O,10%CO_2, 20%H_2,balance He	400	58	0.014	0.34	This work
5Ni5Cu/CeO_2 (1)	7%CO,22%H_2O,10%CO_2, 20%H_2,balance He	410	69	0.012	0.31	This work
5Ni5Cu/CeO_2	7%CO,22%H_2O,10%CO_2, 20%H_2,balance He	350	41.3	0.013	0.33	[54]
Ni/2Na/CeO_2	7% CO, 22% H_2O, 10% CO_2, 20% H_2, balance He	400	-	0.46	-	[13]
Ni/SiO_2	5%CO, 25%H_2O, balance He	375	-	2.79	-	[72]
5 at.% Ni-Ce(10%La)Ox	1%CO,2%H_2O,balance He	275-300	38.2	-	-	[34]
Pd-Cu/CeO_2	9.8%CO,23.0%H_2O,1.4%O_2, balance N_2	220-280	29.1-87.1	0.8-2.08	-	[73]
Pd-Zn/Al_2O_3	6.8%CO,21.9%H_2O,8.5%CO_2, 37.4%H_2	280	75	0.036	-	[74]
Cu (111)	1%CO,2.6%H_2O,balance N_2	340	71	-	0.32	[75]
Cu/ZnO/La	7%CO,23%H_2O,8.5%CO_2, 37.5%H_2,balance N_2	230	31.6-43.1	0.004-0.018	-	[76]
Pt/TiO_2	2.83% CO, 5.66% H_2O, 37.7% H_2, balance He	300	-	0.36	-	[77]
8%CuO/Al_2O_3	7%CO,22%H_2O,8.5%CO_2, 37%H_2,balance Ar	300	62	0.4	-	[78]

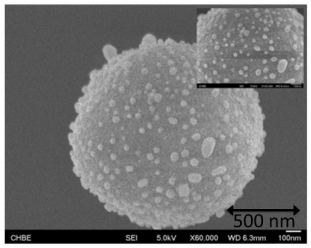

Fig. 6 FESEM image for spent 5Ni5Cu/CeO_2 (3) catalyst after 30 hours of reaction at 450°C.

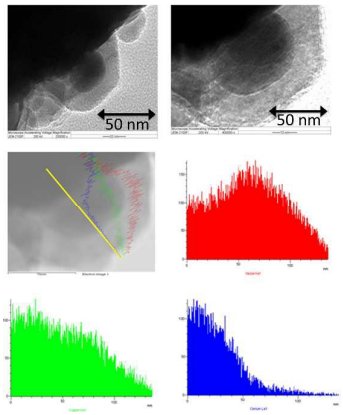

Fig. 7 FETEM-EDX images for spent 5Ni5Cu/CeO_2 (3) catalyst after 30hours of reaction at 450°C.

TPR-CO-MS Measurement

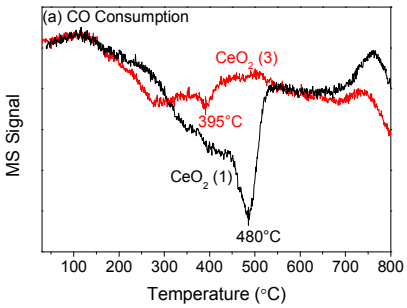

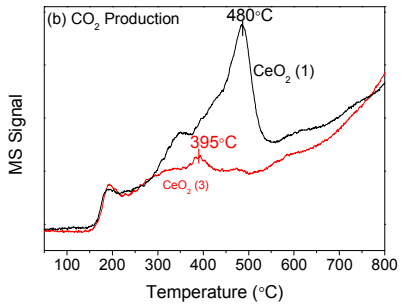

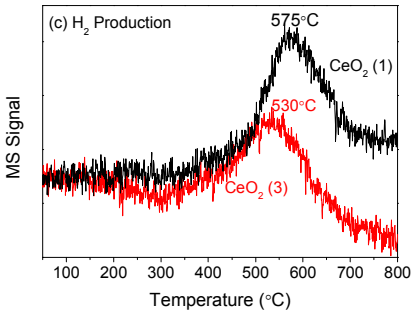

Fig. 8 TPR-CO-MS for (a) CO Consumption; (b) CO_2 Production; (c) H_2 Production.

CO-TPR-MS is a commonly used characterization technique to identify the surface oxygen species and the reactivity of the catalysts toward CO. Four reactions are mainly identified: (i) surface water gas shift reaction, (ii) CO disproportionation, (iii) oxidation of CO by surface lattice oxygen and (iv) the reaction of C-H intermediate species (s-support) with an adsorbed H species on metal surface (M) as listed in equations (1) to (4).[79-81]

$CO\text{-}M + OH\text{-}s \rightarrow 0.5H_2(g) + CO_2(g) + [Ms/e\text{-}]$ (1)

$2CO\text{-}M \rightarrow CO_2(g) + C\text{-}M + M$ (2)

$CO\text{-}M + O_s \rightarrow CO_2(g) + [Ms/e\text{-}]$ (3)

$HCOO\text{-}s + H\text{-}M \rightarrow CO_2(g) + H_2(g) + [Ms/e\text{-}]$ (4)

It can be clearly seen from Figure 8a and 8b that CO consumption and CO_2 production of CeO_2 (3) demonstrates the majority removal of surface oxygen at lower temperature (<400°C) in comparison with CeO_2 (1). Evolution of H_2 is also observed during CO-TPR as shown in Figure 8c. CeO_2 (3) exhibits lower H_2 production temperature (530°C) compared to CeO_2 (1) which H_2 production occurs at 575°C, indicating that surface water gas shift reaction (Eq. 1) proceed. Upon impregnation of Ni-Cu bimetallic onto ceria, 5Ni5Cu-CeO_2 (3) catalyst shows high reactivity towards CO, giving the highest CO consumption and CO_2 production peaks at 475°C (shown in Figure 9a and 9b). This could be possibly that the Ni-Cu alloy has activated the surface lattice oxygen particularly for high temperature reaction based on the Eq. 3.[54]

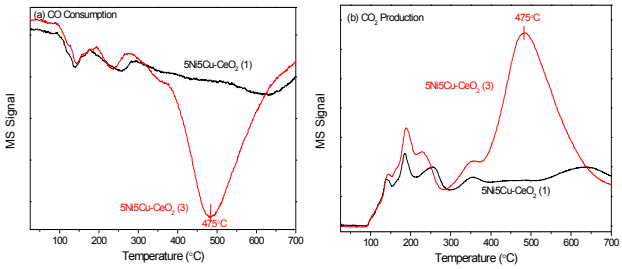

Fig. 9 TPR-CO-MS for (a) CO Consumption and (b) CO_2 Production.

In-situ DRIFTS for CO adsorption

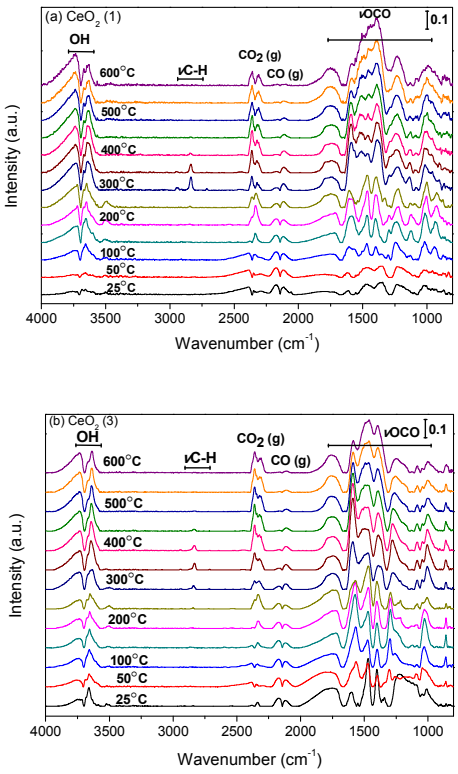

Fig. 10 *In-situ* DRIFTS Spectra for CO adsorption on (a) CeO_2 (1) and (b) CeO_2 (3).

Support

CO adsorption is performed to identify the ceria surface active species in catalysis using *in-situ* DRIFTS spectroscopy. Ceria are firstly outgassed at 250°C for one hour using purified helium and then cooled down to 25°C. 5%CO in 95% helium gas is introduced to investigate the surface properties of ceria from 25°C, 50°C to 600°C with 50°C as the temperature interval. Table 4 summarizes the surface species observed during CO adsorption study. A detailed explanation is explicated as follows.

Figure 10a and 10b display the DRIFTS spectra of CO adsorption study for CeO_2 (1) and CeO_2 (3) respectively. There are three main regions showing the reactive surface species during CO adsorption study, i.e. surface hydroxyl (3800-3500cm^{-1}), surface formate (3000-2700cm^{-1}) and surface carbonate (2000-800cm^{-1}). Three types of hydroxyl groups (type I, type II-A and type III OH group) are observed at low temperature.[82] The intensity of the type III OH group is significantly lower on CeO_2 (3) as compared to CeO_2 (1). Both of the ceria exhibits the same behavior as the function of temperature, the type III hydroxyl group disappeared at temperatures more than 250°C whereas only type I and type II-A hydroxyl group is observed at high temperature. In addition, the intensity of type II-A hydroxyl group is decreased and type I-OH is increased as the temperature increased.[83] Bidentate formate (2945, 2852cm^{-1}) species is also observed for these two different ceria crystal sizes. This species is generally formed via the reaction of CO adsorbed with surface hydroxyl group at low temperature and started to decompose to CO_2 and H_2 as the elevated temperature.[84] CeO_2 (1) displays high intensity of bidentate formate in comparison with CeO_2 (3). This could imply that bidentate formate formed on CeO_2 (3) surface is easily to be decomposed, in line with the finding of CO-TPR-MS profile (Figure 8c). In the surface carbonate region, there is a substantial change in intensity of carbonates species as the elevated temperature. At low CO adsorption temperature, CeO_2 (1) presents a band located at 1025, 1350, 1588 cm^{-1} and are attributed to the naturally available unidentate carbonate whereas no band was seen on CeO_2 (3).[85] At high CO adsorption temperature, bidentate carbonate (1025, 1260, 1570 cm^{-1}) and polydentate carbonates (1066, 1388, 1475 cm^{-1}) species are observed, however an additional band located at 1130, 1244, 1388, 1750 cm^{-1} (which is attributed to bridged carbonate) is formed on CeO_2 (1) and this species is thermally stable up to 600°C.[85]

Reduced Catalysts

The 5Ni5Cu/CeO_2 catalysts were firstly reduced *in-situ* at 450°C and purged with helium to remove the weakly chemisorbed hydrogen before 5%CO in 95% helium gas was introduced. This CO-TPR-MS investigation is crucial in determining the surface properties of catalyst from 25°C, 50°C to 600°C with 50°C as the temperature interval. The surface species observed during CO adsorption study was tabulated in Table 4 and the detailed explanation is discussed as follows. By introducing Ni-Cu bimetallic catalyst onto CeO_2 (1) supports, two types of hydroxyl groups (type I and type II-OH) are clearly observed on reduced 5Ni5Cu/CeO_2 (1) catalyst. At low temperature, mostly type II-A OH group is formed whereas type II-A and type I OH group form at high temperature (above 250°C) as depicted in Figure 11a. The linear adsorption of CO on Cu^+ (2120 cm^{-1}) is likely to be seen at 25°C which may indicate high dispersion of copper entities.[88] As the temperature exceeds 200°C, Ni-Cu alloy is found and showed to be thermally stable up to 500°C with the absorption band from 2040-2010 cm^{-1}.[54] 5Ni5Cu/CeO_2 (3) catalyst also behaves the same characteristic with 5Ni5Cu/CeO_2 (1) catalyst in the surface hydroxyl zone and surface carbonyl zone. In the carbonate region, unidentate carbonate (1050, 1330, 1550 cm^{-1}), the naturally abundant species, carboxylates species (1330, 1500, 1550cm^{-1}) and $\pi(CO_3)$ mode of carbonates (860cm^{-1}) are observed at low temperature CO adsorption on 5Ni5Cu/CeO_2 (1) catalyst. In contrast, bidentate carbonate species are found on 5Ni5Cu/CeO_2 (3) catalyst with no carboxylates species appeared.

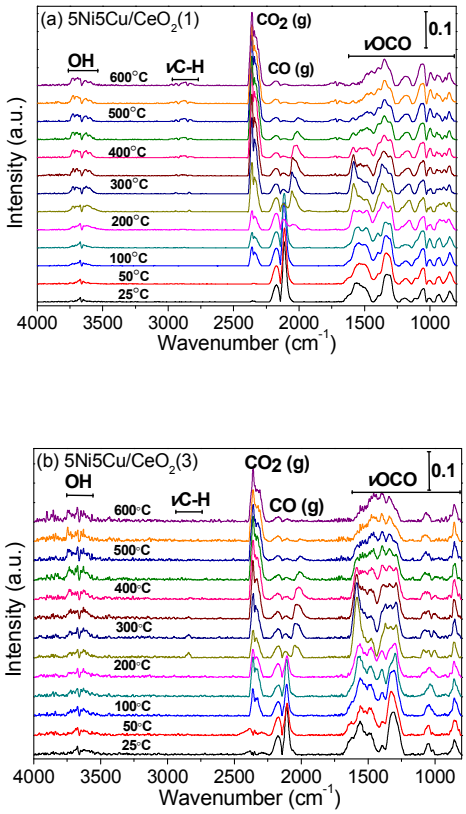

Fig. 11 *In-situ* DRIFTS Spectra for CO adsorption on on (a) 5Ni5Cu/CeO_2 (1) and (b) 5Ni5Cu/CeO_2 (3).

Discussion

Role of CeO_2 support size

Three different particle sizes of ceria as catalyst support were successfully synthesized to investigate the role of CeO_2 in water gas shift reaction. The catalyst activity showed that 5Ni5Cu/CeO_2 (3) catalyst exhibited the highest CO conversion as compared to other catalysts as well as high stability after long term test. The reason is due to the formation of small Ni-Cu alloy crystal size as revealed in XRD measurement, XPS measurement and N_2O decomposition analysis. As can be seen from *in-situ* DRIFTS spectra formate species formed from CO reaction with hydroxyl on ceria, CeO_2(3) exhibited lower intensity as compared to CeO_2 (1). This suggested that the hydroxyl group on CeO_2 (3) is more reactive to react with CO in formate formation and decomposition of formate occur at low temperature than CeO_2 (1) which is in line with the observation from CO-TPR-MS where H_2 production occurred at low temperature. Although CeO_2 (3) catalyst support exhibits low amount of surface lattice oxygen (as discussed in H_2-TPR measurement section); however, with the impregnation of Ni-Cu catalyst, it has promoted catalyst reducibility. Apart from the small crystal size of ceria promotes the reducibility of 5Ni5Cu/CeO_2 (3) catalyst; enhancement of surface lattice oxygen was also evidenced from CO-TPR-MS for 5Ni5Cu/CeO_2

Table 4. CO adsorption study on CeO_2 supports and 5Ni5Cu/CeO_2 catalysts.

Surface species	Wavenumber (cm^{-1})	Catalysts			
	Literature value	CeO_2 (1)	CeO_2 (3)	5Ni5Cu/CeO_2 (1)	5Ni5Cu/CeO_2 (3)
Surface hydroxyl	[86, 87]				
Type I - OH	3710	3709	3710	3710	3710
Type II-A -OH	3650, 3680-3660	3648, 3675	3648, 3675	3650, 3670	3650, 3680
Type III -OH	3500, 3600	3514	3514	-	-
Surface Formate	[84]				
Bidentate	2945,2852, 1558, 1369,1329	2945, 2841, 2710, 1588, 1358	2945, 2840,2710, 1588, 1354	2945, 2840, 1588,1365,1325	2945,2845,1588,1370, 1325
Surface Carbonyl	[88, 89]				
CO adsorb on Ce^{4+}	2177,2156	2178	2178		
CO adsorb on Ce^{3+}	2120-2127	2125	2125	2120 (25°C)	2120 (25°C)
Linear	2160-2080 (Cu^{+}-CO) 2044-2017 (CO on Ni-Cu alloy)	-	-	2040-2010 (250°C)	2040-2000 (250°C)
Surface Carbonate	[90, 91]				
Unidentate	1545, 1348, 1062	1588, 1350, 1025	-	1550, 1330, 1050	1550,1320,1050
Bidentate	1562, 1286, 1028	1570, 1260, 1025	1550,1300,1050	-	1550, 1300,1050
Polydentate	1462, 1353, 1066	1475, 1388, 1066 (450°C)	1498, 1400, 1050 (above 450°C)	1480, 1350, 1050	1470, 1350, 1050
Bridged	1728, 1396, 1219, 1132	1750, 1388, 1244,1130 (above 450°C)	-	-	-
Carboxylate	1560, 1510, 1310	-	-	1550, 1500, 1330	-

(3) catalyst. This can be postulated that the formation of Ni-rich Ni-Cu alloy catalyst structure observed from FETEM-EDX which could be the possible reason to activate the surface lattice oxygen from ceria in catalyzing water gas shift reaction with high activity and stability.

Proposed Reaction Mechanism

The important role of ceria size as catalyst support has shown substantial advantages such as dispersed Ni-Cu alloy and promote surface lattice oxygen. However, the role of ceria crystal size in affecting the reaction mechanism is still not clearly investigated. From the CO adsorption analysis, this can be clearly shown that two types of hydroxyl groups (Type I OH and Type II-A OH) are observed whereas at high temperature only type I-OH group is present. This may indicate that during reduction process, Ni-Cu enhances the reduction of ceria surface. Therefore, this active surface hydroxyl group could react with the adsorbed CO to form active intermediate species. Thereafter, this is replenished by water dissociation onto this oxygen vacancy sites to form surface hydroxyl group. At high adsorption temperature, CO gas tends to adsorb onto the Ni-Cu alloy species and react with the surface hydroxyl group in forming different types of intermediate species such as formate and carboxyl species.[50, 92, 93] From the observation of *in-situ* DRIFTS analysis, formate species are encountered in the *in-situ* DRIFTS spectra for both of 5Ni5Cu/CeO_2 (1) and 5Ni5Cu/CeO_2 (3) catalysts. This shows that there is no significant role of bidentate formate species in the reaction pathway or it may act as spectator or minor role in the reaction pathway.[57] Moreover, several types of carbonate species are clearly noted from the *in-situ* DRIFTS spectra. The only difference is the presence of carboxylate species, assigning to 5Ni5Cu/CeO_2 (1) catalyst whereas only bidentate carbonate species are found on 5Ni5Cu/CeO_2 (3) catalyst. This may imply that carboxylate species are the main species (inhibitor or slow decomposition rate) observed on the catalyst surface, resulting low activity of 5Ni5Cu/CeO_2 (1) catalyst. The proposed carboxylate formation pathway is shown in Figure 12 to predict the possible formation of carboxylate and it depends strongly on the catalyst surface composition particularly for Cu-rich or Ni-rich Ni-Cu alloy formation. Hence, it could be postulated that the decomposition of carboxylate is the slowest step in affecting the catalytic performance of 5Ni5Cu/CeO_2 (1) catalyst which shows Cu-rich Ni-Cu alloy on the catalyst surface.[94] On the other hand, bidentate carbonate species formed on 5Ni5Cu/CeO_2 (3) catalyst might possibly come from the conversion of bidentate formate at high temperature to bidentate carbonate species or might be just a spectator. However, based on *in-situ* DRIFTS analysis alone, it could not be easily to postulate the water gas shift reaction mechanism. A detail study with an advanced spectroscopic and steady-state isotopic transient kinetically analysis should be performed to capture the real intermediate species and determined the "active" or "in-active" species.[94] Based on our recent work, carboxyl species could be the main intermediate species for water gas shift reaction which we have shown by using the kinetic study.[54] Therefore, we would like to propose that carboxylate that found from *in-situ* DRIFTS could be due to the slow decomposition of this species or the intermediate form from the carboxyl, resulting in low catalytic activity observed on 5Ni5Cu/CeO_2 (1) catalyst. The water gas shift reaction mechanism is postulated to be affected by different Ni-Cu surface composition.

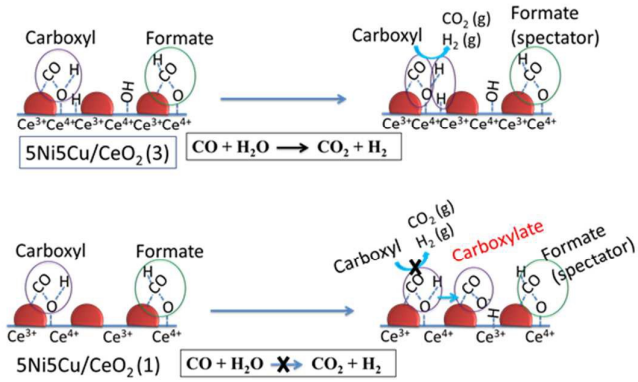

Fig. 12 Postulated carboxylate formation on different CeO_2 crystal sizes in water gas shift reaction.

Conclusions

In this study, CeO_2 nano-spherical particles with different crystal sizes and particle size were successfully synthesized via PVP-assisted hydrothermal method to investigate the role of ceria crystal size as catalyst support for high temperature water gas shift reaction. Several concluding remarks were summarized as below: (a) the decrease of ceria crystal sizes improves the surface metal dispersion, (b) small ceria crystal size enhances the presence of the active hydroxyl group at low temperature, improving the surface water gas shift reaction in hydrogen production. With the well dispersed Ni-Cu alloys, this activates the surface lattice oxygen (CO-TPR-MS) which is taking part in catalyzing water gas shift reaction at high temperature, and (c) Inhibition of carboxylate species onto 5Ni5Cu/CeO_2 (1) catalyst or slow decomposition of carboxylate species is postulated could be the main reason to decrease the catalytic activity. The water gas shift reaction mechanism is strongly depended on the Ni-Cu surface composition rather than the size of Ni-Cu alloys.

Acknowledgements

The authors gratefully appreciate and acknowledge the financial support from the National University of Singapore in providing the research scholarship and NEA agency (NEA-ETRP Grant No. 1002114, RP No. 279-000-333-490) for generously supporting this work. The authors would like to thank Dr J. Ashok, Dr L. Mo, Dr. T. Maneerung and Dr. Y. Kathiraser for their valuable suggestions.

Notes and references

1. C. Sun, H. Li and L. Chen, *Energy & Environmental Science*, 2012, **5**, 8475-8505.
2. L. Zhang, L. Li, Y. Cao, X. Yao, C. Ge, F. Gao, Y. Deng, C. Tang and L. Dong, *Applied Catalysis B: Environmental*, 2015, **165**, 589-598.
3. E. M. Seftel, M. C. Puscasu, M. Mertens, P. Cool and G. Carja, *Applied Catalysis B: Environmental*, 2015, **164**, 251-260.
4. Q. Dai, S. Bai, H. Li, W. Liu, X. Wang and G. Lu, *Applied Catalysis B: Environmental*, 2015, **168–169**, 141-155.
5. F. Lin, R. Delmelle, T. Vinodkumar, B. M. Reddy, A. Wokaun and I. Alxneit, *Catalysis Science & Technology*, 2015, **5**, 3556-3567.
6. B. Penkala, D. Aubert, H. Kaper, C. Tardivat, K. Conder and W. Paulus, *Catalysis Science & Technology*, 2015, **5**, 4839-4848.
7. X.-P. Wu, X.-Q. Gong and G. Lu, *Physical Chemistry Chemical Physics*, 2015, **17**, 3544-3549.
8. J. Ashok and S. Kawi, *International Journal of Hydrogen Energy*, 2013, **38**, 13938-13949.
9. U. Oemar, K. Hidajat and S. Kawi, *Applied Catalysis A: General*, 2011, **402**, 176-187.
10. W. T. Gibbons, T. H. Liu, K. J. Gaskell and G. S. Jackson, *Applied Catalysis B: Environmental*, 2014, **160–161**, 465-479.
11. J. Kugai, J. T. Miller, N. Guo and C. Song, *Applied Catalysis B: Environmental*, 2011, **105**, 306-316.
12. S. Park, J. M. Vohs and R. J. Gorte, *Nature*, 2000, **404**, 265-267.
13. M. L. Ang, U. Oemar, E. T. Saw, L. Mo, Y. Kathiraser, B. H. Chia and S. Kawi, *ACS Catalysis*, 2014, **4**, 3237-3248.
14. X. Wu and S. Kawi, *Crystal Growth & Design*, 2010, **10**, 1833-1841.
15. U. Oemar, M. L. Ang, W. F. Hee, K. Hidajat and S. Kawi, *Applied Catalysis B: Environmental*, 2014, **148–149**, 231-242.
16. J. Ashok, Y. Kathiraser, M. L. Ang and S. Kawi, *Applied Catalysis B: Environmental*, 2015, **172–173**, 116-128.
17. J. Ashok and S. Kawi, *ACS Catalysis*, 2014, **4**, 289-301.
18. J. Ashok and S. Kawi, *Applied Catalysis A: General*, 2015, **490**, 24-35.
19. X. Y. Gao, J. Ashok, S. Widjaja, K. Hidajat and S. Kawi, *Applied Catalysis A: General*, 2015, **503**, 34-42.
20. Z. Li, Y. Kathiraser, J. Ashok, U. Oemar and S. Kawi, *Langmuir*, 2014, **30**, 14694-14705.
21. Z. Li, Y. Kathiraser and S. Kawi, *ChemCatChem*, 2015, **7**, 160-168.
22. Z. Li, L. Mo, Y. Kathiraser and S. Kawi, *ACS Catalysis*, 2014, **4**, 1526-1536.
23. L. Mo and S. Kawi, *Journal of Materials Chemistry A*, 2014, **2**, 7837-7844.
24. L. Mo, K. K. M. Leong and S. Kawi, *Catalysis Science & Technology*, 2014, **4**, 2107-2114.
25. N. Perret, X. Wang, J. J. Delgado, G. Blanco, X. Chen, C. M. Olmos, S. Bernal and M. A. Keane, *Journal of Catalysis*, 2014, **317**, 114-125.
26. J. Yang, L. Lukashuk, J. Akbarzadeh, M. Stöger-Pollach, H. Peterlik, K. Föttinger, G. Rupprechter and U. Schubert, *Chemistry – A European Journal*, 2015, **21**, 885-892.
27. F. Zhou, X. Zhao, H. Xu and C. Yuan, *The Journal of Physical Chemistry C*, 2007, **111**, 1651-1657.
28. K. Kaneko, K. Inoke, B. Freitag, A. B. Hungria, P. A. Midgley, T. W. Hansen, J. Zhang, S. Ohara and T. Adschiri, *Nano Letters*, 2007, **7**, 421-425.
29. Z. Wang, G. Shen, J. Li, H. Liu, Q. Wang and Y. Chen, *Applied Catalysis B: Environmental*, 2013, **138–139**, 253-259.
30. C. R. Jung, A. Kundu, S. W. Nam and H.-I. Lee, *Applied Catalysis B: Environmental*, 2008, **84**, 426-432.
31. C. T. Campbell and C. H. F. Peden, *Science*, 2005, **309**, 713-714.
32. G. B. Sun, K. Hidajat, X. S. Wu and S. Kawi, *Applied Catalysis B: Environmental*, 2008, **81**, 303-312.
33. U. Oemar, P. S. Ang, K. Hidajat and S. Kawi, *International Journal of Hydrogen Energy*, 2013, **38**, 5525-5534.
34. Y. Li, Q. Fu and M. Flytzani-Stephanopoulos, *Applied Catalysis B: Environmental*, 2000, **27**, 179-191.
35. X. Liu, W. Ruettinger, X. Xu and R. Farrauto, *Applied Catalysis B: Environmental*, 2005, **56**, 69-75.
36. C. M. Kalamaras, K. C. Petallidou and A. M. Efstathiou, *Applied Catalysis B: Environmental*, 2013, **136–137**, 225-238.
37. E. T. Saw, U. Oemar, M. L. Ang, K. Hidajat and S. Kawi, *ChemCatChem*, 2015, **7**, 3358-3367.
38. M. Shekhar, J. Wang, W. S. Lee, W. D. Williams, S. M. Kim, E. A. Stach, J. T. Miller, W. N. Delgass and F. H. Ribeiro, *J Am Chem Soc*, 2012, **134**, 4700-4708.
39. P. Panagiotopoulou, A. Christodoulakis, D. I. Kondarides and S. Boghosian, *Journal of Catalysis*, 2006, **240**, 114-125.
40. R. Si and M. Flytzani-Stephanopoulos, *Angewandte Chemie International Edition*, 2008, **47**, 2884-2887.
41. J. Xu, J. Harmer, G. Li, T. Chapman, P. Collier, S. Longworth and S. C. Tsang, *Chemical Communications*, 2010, **46**, 1887-1889.
42. J. Kugai, V. Subramani, C. Song, M. H. Engelhard and Y.-H. Chin, *Journal of Catalysis*, 2006, **238**, 430-440.
43. Z. Wu, M. Li, J. Howe, H. M. Meyer and S. H. Overbury, *Langmuir*, 2010, **26**, 16595-16606.
44. S. Chen, L. Luo, Z. Jiang and W. Huang, *ACS Catalysis*, 2015, **5**, 1653-1662.
45. K. Mudiyanselage, S. D. Senanayake, L. Feria, S. Kundu, A. E. Baber, J. Graciani, A. B. Vidal, S. Agnoli, J. Evans, R. Chang, S. Axnanda, Z. Liu, J. F. Sanz, P. Liu, J. A. Rodriguez and D. J. Stacchiola, *Angewandte Chemie International Edition*, 2013, **52**, 5101-5105.
46. J. Wang, V. F. Kispersky, W. Nicholas Delgass and F. H. Ribeiro, *Journal of Catalysis*, 2012, **289**, 171-178.
47. L. Barrio, A. Kubacka, G. Zhou, M. Estrella, A. Martínez-Arias, J. C. Hanson, M. Fernández-García and J. A. Rodriguez, *Journal of Physical Chemistry C*, 2010, **114**, 12689-12697.
48. J. H. Pazmiño, M. Shekhar, W. Damion Williams, M. Cem Akatay, J. T. Miller, W. Nicholas Delgass and F. H. Ribeiro, *Journal of Catalysis*, 2012, **286**, 279-286.
49. F. Zhao, Z. Liu, W. Xu, S. Yao, A. Kubacka, A. C. Johnston-Peck, S. D. Senanayake, A.-Q. Zhang, E. A. Stach, M. Fernández-García and J. A. Rodriguez, *The Journal of Physical Chemistry C*, 2014, **118**, 2528-2538.
50. A. A. Gokhale, J. A. Dumesic and M. Mavrikakis, *Journal of the American Chemical Society*, 2008, **130**, 1402-1414.

51. S. Aranifard, S. C. Ammal and A. Heyden, *The Journal of Physical Chemistry C*, 2014, **118**, 6314-6323.
52. G. Jacobs and B. H. Davis, *Applied Catalysis A: General*, 2007, **333**, 192-201.
53. C. M. Kalamaras, S. Americanou and A. M. Efstathiou, *Journal of Catalysis*, 2011, **279**, 287-300.
54. E. T. Saw, U. Oemar, X. R. Tan, Y. Du, A. Borgna, K. Hidajat and S. Kawi, *Journal of Catalysis*, 2014, **314**, 32-46.
55. E. T. Saw, U. Oemar, X. R. Tan, Y. Du, A. Borgna, K. Hidajat and S. Kawi, *Journal of Catalysis*, 2014, **314**, 32-46.
56. R. M. Koros and E. J. Nowak, *Chemical Engineering Science*, 1967, **22**, 470.
57. R. J. Madon, D. Braden, S. Kandoi, P. Nagel, M. Mavrikakis and J. A. Dumesic, *Journal of Catalysis*, 2011, **281**, 1-11.
58. S. T. Oyama, X. Zhang, J. Lu, Y. Gu and T. Fujitani, *Journal of Catalysis*, 2008, **257**, 1-4.
59. J. Ashok, Y. Kathiraser, M. L. Ang and S. Kawi, *Catalysis Science & Technology*, 2015, **5**, 4398-4409.
60. N. Laosiripojana and S. Assabumrungrat, *Applied Catalysis B: Environmental*, 2005, **60**, 107-116.
61. H. C. Yao and Y. F. Y. Yao, *Journal of Catalysis*, 1984, **86**, 254-265.
62. M. F. L. Johnson and J. Mooi, *Journal of Catalysis*, 1987, **103**, 502-505.
63. A. Trovarelli, C. Deleitenburg, G. Dolcetti and J. L. Lorca, *Journal of Catalysis*, 1995, **151**, 111-124.
64. L. Kundakovic and M. Flytzani-Stephanopoulos, *Applied Catalysis A: General*, 1998, **171**, 13-29.
65. F. Zhang, S.-W. Chan, J. E. Spanier, E. Apak, Q. Jin, R. D. Robinson and I. P. Herman, *Applied Physics Letters*, 2002, **80**, 127-129.
66. M. L. Ang, U. Oemar, Y. Kathiraser, E. T. Saw, C. H. K. Lew, Y. Du, A. Borgna and S. Kawi, *Journal of Catalysis*, 2015, **329**, 130-143.
67. M. Trudeau, A. Tschöpe and J. Ying, *Surface and interface analysis*, 1995, **23**, 219-226.
68. X.-D. Zhou and W. Huebner, *Applied Physics Letters*, 2001, **79**, 3512-3514.
69. A. R. Naghash, T. H. Etsell and S. Xu, *Chemistry of Materials*, 2006, **18**, 2480-2488.
70. L. Guczi, Z. Schay, G. Stefler, L. F. Liotta, G. Deganello and A. M. Venezia, *Journal of Catalysis*, 1999, **182**, 456-462.
71. L.-Y. Gan, R.-Y. Tian, X.-B. Yang, H.-D. Lu and Y.-J. Zhao, *The Journal of Physical Chemistry C*, 2012, **116**, 745-752.
72. J. Ashok, M. L. Ang, P. Z. L. Terence and S. Kawi, *ChemCatChem*, 2016, DOI: 10.1002/cctc.201501284, n/a-n/a.
73. J. Kugai, E. B. Fox and C. Song, *Applied Catalysis A: General*, 2013, **456**, 204-214.
74. L. Bollmann, J. L. Ratts, A. M. Joshi, W. D. Williams, J. Pazmino, Y. V. Joshi, J. T. Miller, A. J. Kropf, W. N. Delgass and F. H. Ribeiro, *Journal of Catalysis*, 2008, **257**, 43-54.
75. C. T. Campbell and K. A. Daube, *Journal of Catalysis*, 1987, **104**, 109-119.
76. R. Kam, C. Selomulya, R. Amal and J. Scott, *Journal of Catalysis*, 2010, **273**, 73-81.
77. X. Zhu, M. Shen, L. L. Lobban and R. G. Mallinson, *Journal of Catalysis*, 2011, **278**, 123-132.
78. A. A. P. N.A. Koryabkina, W.F. Ruettinger, R.J. Farrauto, and F.H. Ribeiro, *Journal of Catalysis*, 2003, **217**, 233-239.
79. H. Zhu, Z. Qin, W. Shan, W. Shen and J. Wang, *Journal of Catalysis*, 2004, **225**, 267-277.
80. A. Bueno-López, K. Krishna, M. Makkee and J. A. Moulijn, *Journal of Catalysis*, 2005, **230**, 237-248.
81. T. Ioannides and X. Verykios, *Journal of Catalysis*, 1993, **140**, 353-369.
82. W. Thitsartarn and S. Kawi, *Green Chemistry*, 2011, **13**, 3423-3430.
83. P. O. Graf, D. J. M. de Vlieger, B. L. Mojet and L. Lefferts, *Journal of Catalysis*, 2009, **262**, 181-187.
84. O. Pozdnyakova, D. Teschner, A. Wootsch, J. Kröhnert, B. Steinhauer, H. Sauer, L. Toth, F. C. Jentoft, A. Knop-Gericke, Z. Paál and R. Schlögl, *Journal of Catalysis*, 2006, **237**, 1-16.
85. P. Bazin, O. Saur, J. C. Lavalley, M. Daturi and G. Blanchard, *Physical Chemistry Chemical Physics*, 2005, **7**, 187-194.
86. F. Zhang, P. Wang, J. Koberstein, S. Khalid and S.-W. Chan, *Surface Science*, 2004, **563**, 74-82.
87. C. Binet, M. Daturi and J.-C. Lavalley, *Catalysis Today*, 1999, **50**, 207-225.
88. P. Gawade, B. Mirkelamoglu and U. S. Ozkan, *The Journal of Physical Chemistry C*, 2010, **114**, 18173-18181.
89. A. Kitla, O. Safonova and K. Föttinger, *Catalysis Letters*, 2013, **143**, 517-530.
90. C. Li, Y. Sakata, T. Arai, K. Domen, K.-i. Maruya and T. Onishi, *Journal of the Chemical Society, Faraday Transactions 1: Physical Chemistry in Condensed Phases*, 1989, **85**, 929-943.
91. C. Li, Y. Sakata, T. Arai, K. Domen, K.-i. Maruya and T. Onishi, *Journal of the Chemical Society, Faraday Transactions 1: Physical Chemistry in Condensed Phases*, 1989, **85**, 1451-1461.
92. G. Jacobs, L. Williams, U. Graham, D. Sparks and B. H. Davis, *The Journal of Physical Chemistry B*, 2003, **107**, 10398-10404.
93. T. Shido, K. Asakura and Y. Iwasawa, *Journal of Catalysis*, 1990, **122**, 55-67.
94. D. W. Flaherty, W.-Y. Yu, Z. D. Pozun, G. Henkelman and C. B. Mullins, *Journal of Catalysis*, 2011, **282**, 278-288.

Faculty of Engineering
Department of Chemical and Biomolecular Engineering

National University of Singapore

For Tables of Contents:

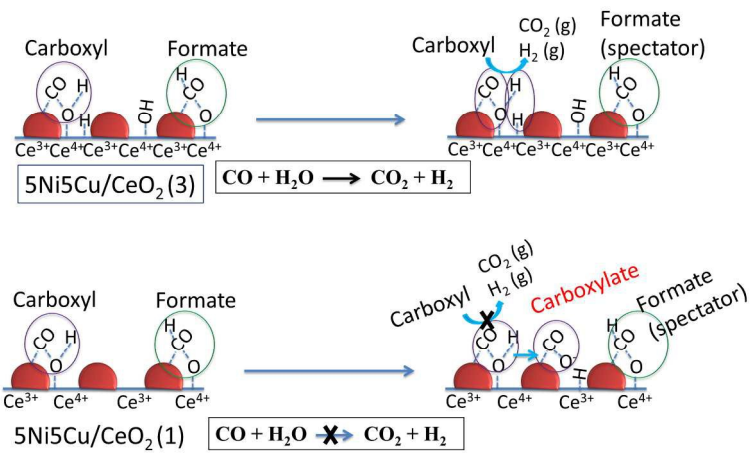

WGS mechanism is strongly depended on the Ni-Cu surface composition

4 Engineering Drive 4, Singapore 117585 Tel: (65) 6516 6312 Fax: (65) 6779 1936
E-mail: chekawis@nus.edu.sg Website: http://www.nus.edu.sg